

# MaSS13K: A Matting-level Semantic Segmentation Benchmark

Chenxi Xie<sup>1,2</sup> Minghan Li<sup>1,2</sup> Hui Zeng<sup>2</sup> Jun Luo<sup>2</sup> Lei Zhang<sup>1,2\*</sup>  
<sup>1</sup>The Hong Kong Polytechnic University <sup>2</sup>OPPO Research Institute

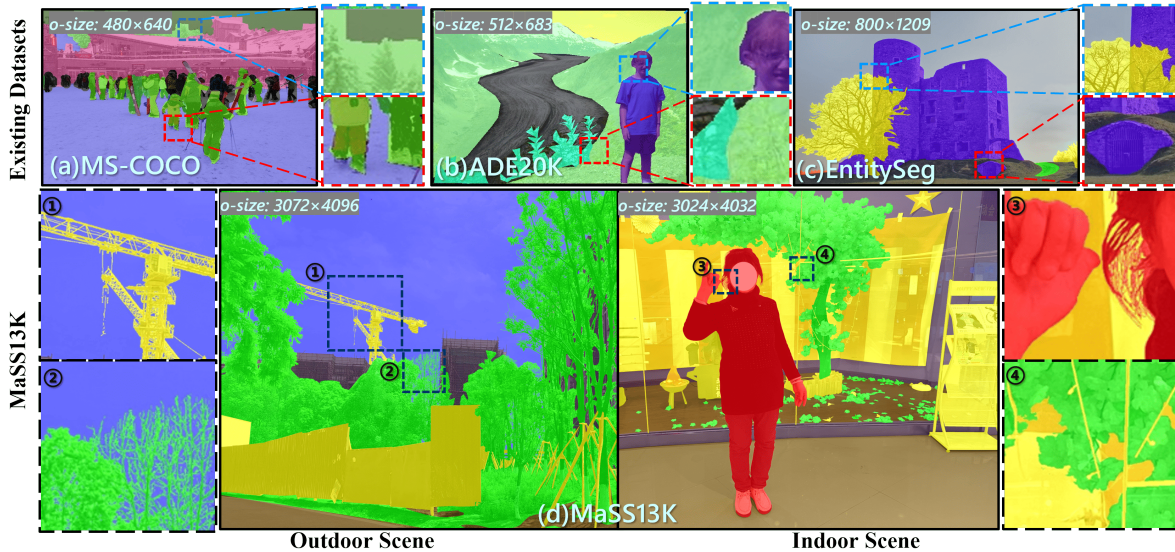


Figure 1. Comparisons on the resolution and annotation quality between existing semantic segmentation datasets (a) COCO, (b) ADE20K, (c) EntitySeg and (d) our established dataset MaSS13K. Note that the ‘others’ category, which is highlighted in yellow, in our MaSS13K actually contains a group of well-segmented objects without specific class names. Please zoom-in for a better view.

## Abstract

High-resolution semantic segmentation is essential for applications such as image editing, bokeh imaging, AR/VR, etc. Unfortunately, existing datasets often have limited resolution and lack precise mask details and boundaries. In this work, we build a large-scale, matting-level semantic segmentation dataset, named MaSS13K, which consists of 13,348 real-world images, all at 4K resolution. MaSS13K provides high-quality mask annotations of a number of objects, which are categorized into seven categories: human, vegetation, ground, sky, water, building, and others. MaSS13K features precise masks, with an average mask complexity 20-50 times higher than existing semantic segmentation datasets. We consequently present a method specifically designed for high-resolution semantic segmentation, namely MaSSFormer, which employs an efficient pixel decoder that aggregates high-level semantic features and low-level texture features across three stages, aiming

to produce high-resolution masks with minimal computational cost. Finally, we propose a new learning paradigm, which integrates the high-quality masks of the seven given categories with pseudo labels from new classes, enabling MaSSFormer to transfer its accurate segmentation capability to other classes of objects. Our proposed MaSSFormer is comprehensively evaluated on the MaSS13K benchmark together with 14 representative segmentation models. We expect that our meticulously annotated MaSS13K dataset and the MaSSFormer model can facilitate the research of high-resolution and high-quality semantic segmentation. Datasets and codes can be found at <https://github.com/xiechenxi99/MaSS13K>.

## 1. Introduction

Semantic segmentation, which assigns a category label to each pixel in an image, has made significant strides over the past decades, driven by the advancements of deep learning and the availability of large-scale benchmark datasets such as COCO-Stuff [30], and ADE20K [57], among others.

\*Corresponding author. This work is supported by the PolyU-OPPO Joint Innovative Research Center.

Building upon these datasets, researchers have developed a variety of networks, including FCN-based models [35] such as the DeepLab series [5, 6]. More recently, with the introduction of transformer architectures [33, 44], transformer-based models [7, 9] have shifted the paradigm of semantic segmentation from pixel-level classification to mask-level classification, achieving new state-of-the-art performance.

The image resolution in COCO-Stuff, ADE20K, and Pascal VOC datasets, however, is commonly below  $1000 \times 1000$ . As the resolution of images encountered in our daily life has significantly risen, there is a growing demand for high-resolution semantic segmentation in applications such as image editing [13], bokeh imaging [23], image retouching [34], AR/VR [26], *etc.*, where fine-scale mask details significantly impact user experience. Recognizing the limitations of low-resolution data, researchers have started to construct some higher-resolution datasets such as Mapillary Vistas [37] and EntitySeg [40]. However, these still fall short with resolutions below 2K and struggle to annotate objects with complex structures and details accurately, as illustrated in Fig. 1. Some datasets, like the DIS [41] and matting datasets [24, 27, 28], are meticulously annotated but they are designed for class-agnostic binary segmentation tasks, which can only be used to differentiate the foreground from the background, rather than parsing the entire scene into semantic categories. Therefore, there remains a demand for highly accurate semantic segmentation datasets to advance the development of high-resolution segmentation models.

To this end, we introduce the **Matting-level Semantic Segmentation** dataset, namely **MaSS13K**, which comprise 13,348 4K-resolution images captured from the real-world scenes. MaSS13K provides exceptionally high-quality annotations (please refer to Fig. 1) on a variety of objects, which are categorized into seven common semantic categories, including ‘human’, ‘vegetation’, ‘ground’, ‘sky’, ‘water’, ‘buildings’ and ‘others’. It should be noted that ‘*others*’ in MaSS13K is not the ‘background’ class in other datasets. It actually refers to a group of well-segmented objects such as the ‘crane’ in Fig. 1. Using the mIPQ [39] score to assess mask complexity, MaSS13K’s mIPQ is 20 to 50 times higher than that of existing semantic segmentation datasets and three times higher than the finely annotated DIS dataset [41]. With MaSS13K, we conduct a comprehensive analysis on 14 representative semantic segmentation methods [2, 6, 7, 9, 18, 20, 38, 43, 45, 48, 51–53, 55]. We show that while these methods achieve satisfactory overall accuracy, they struggle with capturing fine boundary details and impose significant computational and memory demands for high-resolution inputs. There is a high demand for developing new semantic segmentation methods, which can balance the computational cost and segmentation performance in high-resolution contexts.

To tackle the above-mentioned challenges, we propose a Transformer-based model, namely MaSSFormer, specifically designed for high-resolution semantic segmentation. We analyze the traditional FPN-based [31] pixel-decoder in the context of high-resolution input, and devise a lightweight pixel-decoder to balance the computational consumption while generating high-quality masks with fine boundaries. In specific, the decoding process is divided into two branches. In the high-level global semantic branch, we efficiently aggregate high-level semantic features across layers, providing robust global context. Moreover, we balance detail and semantic information by expanding the receptive field to capture multi-scale structures. In the low-level local structure branch, we extract edge-aware features to enhance detail segmentation accuracy. With the guidance of edge detection, we fuse the features in the two branches and generate the final feature with accurate details. Extensive experiments on MaSS13K dataset demonstrate that our proposed MaSSFormer outperforms existing semantic segmentation methods, particularly in boundary quality.

While the MaSS13K dataset contains seven classes, its highly detailed semantic annotations enable networks to learn the general ability to accurately segment regions based on class-agnostic boundaries. To validate this point, we develop a simple yet effective training pipeline that uses powerful pre-trained models to generate low-quality pseudo-labels for new classes, which are then combined with our finely annotated labels to train MaSSFormer. Our experiments show that MaSSFormer can produce higher-quality masks for these newly introduced classes, effectively transferring its fine segmentation abilities to novel categories. This highlights the significant potential of the meticulously annotated MaSS13K dataset for advancing future research in high-resolution and high-quality semantic segmentation.

Our contributions are summarized as follows:

- We introduce MaSS13K, a large-scale semantic segmentation dataset, containing 13K 4K-resolution images with ultra-high quality semantic annotations.
- We propose a simple yet effective baseline MaSSFormer for high-resolution semantic segmentation, which surpasses existing methods, particularly in boundary quality.
- We devise a pipeline to empower the model with the capacity to accurately segment novel classes of objects without extra human efforts, revealing the potential of the high-quality semantic annotations in MaSS13K for future high-resolution segmentation research.
- We conduct a comprehensive benchmarking on the MaSS13k dataset by evaluating MaSSFormer with 14 cutting-edge semantic segmentation methods.

## 2. Related Work

**Image Segmentation Datasets.** Numerous segmentation datasets have been developed recently, generally falling

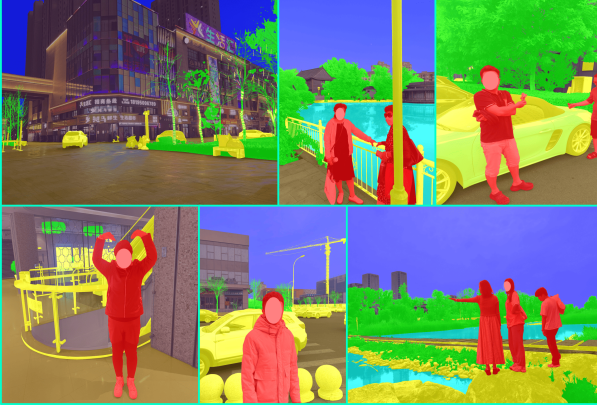


Figure 2. Some typical scenes in our MaSS13K dataset.

into two categories: multi-class and binary segmentation datasets. Multi-class datasets are primarily designed for tasks such as semantic segmentation [19], instance segmentation [21], and panoptic segmentation [15]. They focus on high-level semantics within scenes and are typically large in scale, encompassing a variety of semantic categories, such as COCO [30] and ADE20K [57], EntitySeg [40], Cityscapes [12] and others [16, 37]. However, these datasets often suffer from lower resolution and poor annotation quality. On the other hand, binary segmentation datasets focus on tasks like salient object detection (SOD) [49, 54], camouflaged object detection (COD) [17, 50], and image matting [28]. They emphasize low-level structures of target objects with fine annotations but are class-agnostic and object-centric, making them unsuitable for full scene parsing. Our MaSS13K addresses these limitations and integrates the strengths of both types of datasets. It includes a range of semantic categories, providing comprehensive coverage of entire scenes. Additionally, it offers high-resolution and matting-level annotations, surpassing the accuracy of existing datasets.

**Semantic Segmentation Methods.** With the development of deep learning, semantic segmentation has made significant progress. Initially, FCN-based [35] methods dominate the field, with notable methods including DeepLab series [3–5], PSPNet [56], OCRNet [53] and some other efficient methods [51, 52]. These methods introduce various modules to aggregate multi-scale semantic information, classifying each pixel directly. With the rise of Transformers and their application in object detection [1], unified mask classification frameworks such as MaskFormer [2, 7, 9] have been proposed for multiple segmentation tasks. This approach decouples mask prediction from classification, achieving impressive performance. However, due to the limitations of existing semantic segmentation datasets, these methods are mostly designed for low-resolution data, resulting in challenges when applied to high-resolution datasets, such as the difficulties in global semantic awareness and poor bound-

Table 1. Statistical comparison between MaSS13K and other segmentation datasets. ‘SS’ denotes semantic segmentation and ‘BS’ denotes binary segmentation. ‘#Size’ indicates the diagonal length. The values are presented as mean  $\pm$  standard deviation.

Type	Dataset	#Image	#Size	#Classes	#IPQ
SS	COCO-Stuff [30]	118K	762 $\pm$ 70	171	7 $\pm$ 4
	ADE20K [57]	20K	667 $\pm$ 227	150	17 $\pm$ 10
	Cityscapes [12]	3K	2290 $\pm$ 0	19	18 $\pm$ 7
	EntitySeg [40]	11K	2684 $\pm$ 2240	151	20 $\pm$ 29
BS	BIG [10]	0.3K	4655 $\pm$ 1312	1	21 $\pm$ 63
	HRSOD [54]	2K	4405 $\pm$ 1631	1	6 $\pm$ 13
	UHRSD [49]	6K	6185 $\pm$ 1332	1	7 $\pm$ 9
	DIS5K [41]	5K	4041 $\pm$ 1618	1	116 $\pm$ 452
SS	MaSS13K	13K	5144 $\pm$ 492	7	383 $\pm$ 818

ary details. While some methods have considered edges [29, 46, 51], they focus on how to use edges to differentiate semantic regions rather than improving boundary and detail segmentation quality. Unlike previous methods, our MaSSFormer is designed to tackle the challenges of high-resolution semantic segmentation, ensuring semantic accuracy while producing segmentation maps with precise detail and sharp boundaries.

### 3. MaSS13K Dataset

**Data Collection.** To address the shortage of high-resolution semantic segmentation data, we construct a large-scale dataset, which consists of 13,348 images of 4K resolution of real-world scenes. These images were captured by various smartphones, including iPhone 14 Pro, Huawei P50, Huawei Mate50, OPPO Find X5, OPPO Reno 8, Vivo X80, and Xiaomi 12, and under different lighting conditions, weather states, and times of day. The images encompass a diverse range of indoor and outdoor scenes, including urban areas, natural landscapes, street views, wilderness, parks, mall interiors, and other public spaces. The diverse sources of data collection not only enhance the dataset’s scene diversity but also improve the segmentation model’s adaptability to different environmental conditions. The snapshots of some typical image scenes are shown in Fig. 2. Note that all images have undergone rigorous ethical and privacy reviews to ensure privacy regulations, and a screening process to remove lower quality pictures.

**Data Annotation.** Each image is annotated with pixel-level precision to create accurate semantic segmentation masks for seven categories: ‘human’, ‘water’, ‘vegetation’, ‘building’, ‘ground’, ‘sky’ and ‘others’. An experienced team was invited to conduct this annotation using the editing tools in PhotoShop. For each of the seven categories, annotators were asked to perform matting-level labeling, focusing on accurate boundary delineation of fine features like hair, leaf edges, and intricate object contours. Afterward, each annotated image went through a multi-stage quality control process, including peer review and final check by senior annotators, to ensure the labeling accu-

racy and consistency.

It should be noted that the ‘others’ category in our MaSS13K dataset is different from the ‘background’ class in other semantic segmentation datasets [16, 30, 57]. In our dataset, the category ‘others’ actually contains a group of accurately segmented objects but without specified class names. As shown by the yellow color in Fig. 1, the masks of the ‘others’ regions are in rich details. Therefore, they are treated as a unique class in our training and evaluation.

**Statistics Analysis.** To better understand the statistics and advantages of our proposed MaSS13K dataset, we compare it against four popular semantic segmentation datasets, including COCO-Stuff [30], ADE20K [57], Cityscapes [12]) and EntitySeg [40], and four datasets used for high-quality binary segmentation (HQBS), including HRSOD [54], UHRSD [49], DIS5K [41] and BIG [10]. We comprehensively compare these datasets in several important attributes for high-resolution segmentation tasks, including dataset size, spatial size, number of categories and mask complexity. Inspired by [41], we also use the mean isoperimetric inequality quotient (mIPQ) [39] metric to measure the overall complexity of masks in an image:  $mIPQ = \frac{1}{4\pi n} \sum_{i=1}^n \frac{L_i^2}{A_i}$ , where  $L^i$  and  $A_i$  denote the mask perimeter and the region area for the  $i$ th category, and  $n$  denotes the total number of categories in this image.

The statistics are presented in Tab. 1. We can see that our dataset has a much higher average diagonal length, which can well represent image resolution, than existing semantic segmentation datasets. Higher resolution allows clearer and more detailed edges to be discerned. While the HQBS datasets also have high resolution, our dataset surpasses them in the number of images and the number of object categories. In addition, MaSS13K has a very small variance in image resolution, indicating a more consistent image quality. In terms of the mIPQ metric, our dataset is 20 times more complex than the EntitySeg dataset, which is known for its high-quality annotations. Even compared to the most finely labeled HQBS dataset DIS5K, our MaSS13K still exceeds it by a significant margin.

## 4. High-Resolution Segmentation Model

### 4.1. Overview of MaSSFormer

Our segmentation model, namely MaSSFormer, is built upon the architecture of Mask2Former [7], as illustrated in Fig. 3. The network consists of three main components: a pixel encoder, a pixel decoder, and a transformer decoder. Specifically, for an input image  $I \in \mathbb{R}^{3 \times H \times W}$  with height  $H$  and width  $W$ , the pixel encoder generates pixel embeddings  $\{F_i\}_{i=1}^4$ , which are then fed into the pixel decoder to produce multi-scale mask features  $\{D_i\}_{i=1}^4$ . Multi-scale mask features are used to update learnable queries through the Transformer decoder. The updated queries are then

passed through MLP layers to generate mask embeddings and class embeddings, which are combined with  $D_1$  to produce the final semantic segmentation results. In this work, we focus on the design of pixel decoder to accommodate high-resolution inputs and generate high-quality mask prediction with precise details.

In our pixel decoder, we use SE block with channel-attention [22] to squeeze the dimension of input pixel embeddings  $\{F_i\}_{i=1}^4$  and obtain squeezed features  $\{S_i\}_{i=1}^4$  of resolution  $\{\frac{H}{k} \times \frac{W}{k}, k = 4, 8, 16, 32\}$ . There are two key challenges for high-resolution and accurate semantic segmentation. First, for high-resolution inputs, the receptive field becomes relatively small, making the *aggregation of high-level semantics difficult*. Second, *precise object edges and fine details* are difficult to extract accurately. To address these challenges, we divide  $\{S_i\}_{i=1}^4$  and image  $I$  into two groups:  $\{S_2, S_3, S_4\}$  and  $\{S_1, I\}$ , and aggregate these features with two parallel branches to obtain global semantics and local details, respectively. In the first branch, we use a Cross Semantic Transmission (CST) module to aggregate global context while generating features with larger spatial resolution. We further introduce a Receptive Field Broaden (RFB) module to expand the receptive field while capturing multi-scale information. In the second branch, we introduce a Low-level Structure Extraction (LSE) module to directly capture high-resolution features with details. Finally, an Edge Guided Fusion (EGF) module is employed to fuse the outputs of the two branches and efficiently produce high-resolution features for mask prediction.

### 4.2. Network Design Details

**Global Semantic Branch.** As shown in Fig. 3, we design a CST module to aggregate global semantic information. Inspired by [2, 56], we apply global average pooling and a  $1 \times 1$  convolution layer on  $F_4$ , and add it to  $S_4$  to enhance the global context. Then, the context-enhanced features are fed into a deformable convolution layer with batch normalization and ReLU activation to obtain feature  $D_4$ , which contains global semantics but with a small spatial size. In contrast,  $S_3$  shares similar semantics with  $S_4$  while offering higher spatial resolution. We use Cross-Attention to transfer the detailed information from  $S_3$  to  $D_4$ , followed by a Feed-Forward Network (FFN)  $FFN(\cdot)$ . To reduce the computational cost, attention is performed within non-overlap windows. After passing through FFN, Self-Attention is computed within the window to further enhance semantic information at higher resolutions. Finally, another FFN is applied, followed by a deformable convolution to expand the receptive field. The whole process can be expressed as:

$$\hat{D}_4 = FFN(CAttn(f_q(US_2(D_4)), f_{k,v}(S_3))), \quad (1)$$

$$D_3 = DCN(FFN(SAtn(f_{g,k,v}(\hat{D}_4))), \quad (2)$$

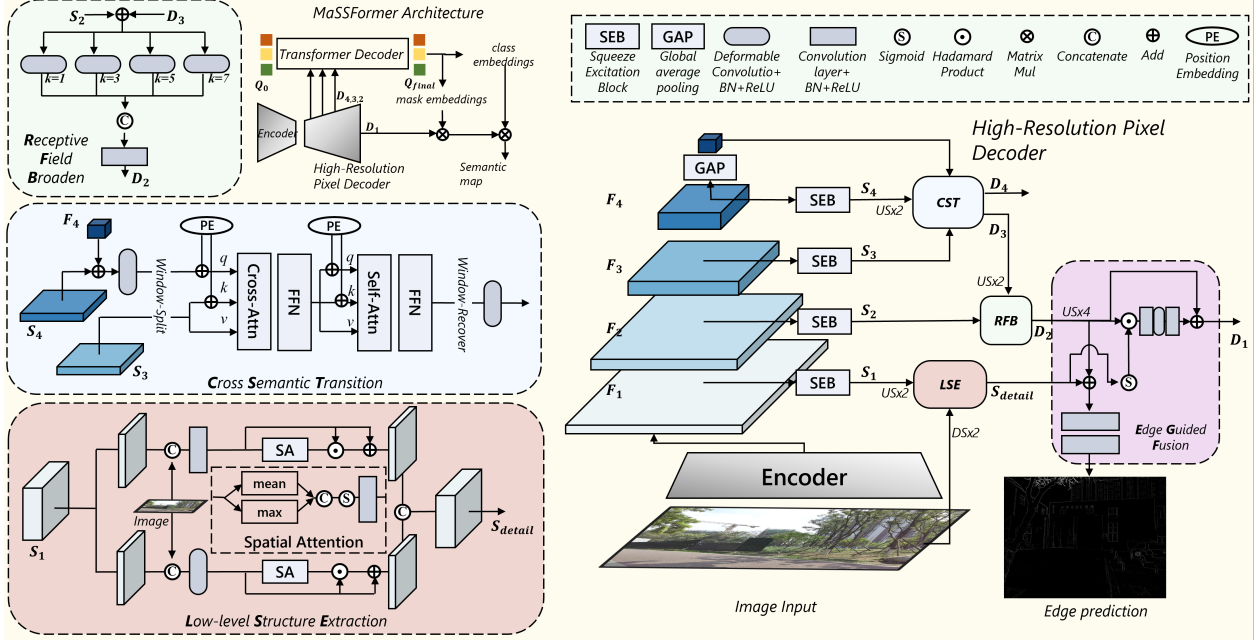


Figure 3. Architecture of MaSSFormer. The model architecture is shown on the top left corner, including the image encoder, pixel decoder and transformer decoder. The detailed structure of the high-resolution pixel decoder is shown on the right of this figure.

where  $f_{\{qkv\}}$  is linear projection and  $US_n(\cdot)$  means up-sampling with factor  $n$ . By computing on low-resolution features, CST can gather global semantics at a lower computational cost and expand to larger spatial resolutions.

We then up-sample the CST output feature  $D_3$  and add it to  $S_2$  before feeding them to the RFB module for higher resolution semantic features  $D_2$ :

$$D_2 = \text{RFB}(US_2(D_3) + S_2). \quad (3)$$

As shown in Fig. 3, the RFB module includes 4 parallel deformable convolution modules with different kernel sizes  $[1, 3, 5, 7]$  and a  $1 \times 1$  point-wise convolution. What’s more, RFB can capture multi-scale structure by setting convolution modules with different kernel size.

**Local Structure Branch.** Traditional semantic segmentation methods [6, 7, 9] typically do not consider high-resolution features for computational efficiency, which is unsuitable for high-resolution semantic segmentation. In this paper, we design the LSE module to extract low-level structure information with low computational cost. To generate high-quality masks, we upsample  $S_1$  with resolution  $\frac{H}{4} \times \frac{H}{4}$  to  $\frac{H}{2} \times \frac{H}{2}$  and incorporate the down-sampled image to directly capture low-level features. However, the resolution of  $\frac{H}{2} \times \frac{H}{2}$  results in a quadratic computational burden. As shown in Fig. 3, we split the input into two sets of features with fewer channels, each concatenated with the image to learn distinctive features. We then use spatial attention [47] to activate and extract low-level structural information. Finally, the features are concatenated and passed

through a  $1 \times 1$  convolution to output high-resolution features  $S_{detail}$ .

**Edge Guided Fusion.** To reduce the cost in fusing low-level structure features at resolution  $\frac{H}{2} \times \frac{W}{2}$ , we design an EGF module to efficiently aggregate detailed information. First, we apply consecutive  $1 \times 1$  convolutions to predict edges  $P^{edge} \in \mathbb{R}^{1 \times H \times W}$  as follows:

$$P^{edge} = \text{Conv}(\text{CBR}(S_{detail} + D_2)), \quad (4)$$

where Conv means convolution and CBR means convolution with batch-norm and ReLU. During training, the edge detection task forces the network to learn the low-level structures of the image, allowing  $S_{detail}$  to receive feedback and focus on edge regions. Then we use  $S_{detail}$  to refine  $D_2$ , which can be expressed as:

$$D_2^{refine} = \text{Sigmoid}(S_{detail}) \times D_2. \quad (5)$$

As shown in Fig. 3, after reducing the channels with a  $1 \times 1$  convolution, we apply a deformable convolution and restore the expanded channels with another  $1 \times 1$  convolution. Finally, a residual connection is used to output high-resolution features  $D_1$ . The intermediate features  $\{D_2, D_3, D_4\}$  are then fed into the transformer decoder.

**Loss Function.** We adopt the loss of Mask2Former [7], which includes classification loss  $L_{cls}$  and mask loss  $L_{mask}$  (a combination of BCE loss and Dice loss). We assign an extra weight in the mask loss to highlight supervision on edge regions. The weights map for each target label  $i$  can be generated using ground-truth label

by  $W^i = G^i - f_{avg}(G^i, k)$ , where  $f_{avg}(\cdot, k)$  is an averaging filter with kernel size  $k$  and  $G^i$  is the  $i$ -th binary ground truth label. We assign the weights for the BCE loss as  $L_{BCE}^w = \frac{1}{mn} \sum_i^n \sum_j^m l_{bce}(P_j^i, G_j^i)(1 + \lambda W_j^i)$ , where  $i, j$  represent the  $j$ -th pixel on the  $i$ -th map and  $\lambda$  is a hyperparameter that adjusts the weight ratio. Additionally, we incorporate an edge detection task in the BCE loss to supervise the edge prediction results, denoted by  $L_{edge} = \frac{1}{n} \sum_i^n l_{bce}(P_i^{edge}, G_i^{edge})$ , where  $G^{edge}$  represents the edges between different semantic regions in the ground truth. The overall loss function is formulated as:

$$L_{total} = L_{BCE}^w + L_{Dice} + L_{cls} + L_{edge}. \quad (6)$$

### 4.3. Segmentation on New Classes

Though our MaSS13K dataset consists of six commonly used categories and an ‘others’ category, the ‘others’ category actually contains various well segmented but unnamed objects. To fully exploit the precise segmentations of those objects in our dataset, we present a novel pipeline to enable MaSSFormer to segment higher-quality masks for new classes beyond the six predefined categories.

We start with the image training set  $\{I_i\}_{i=1}^n$  and the corresponding annotation set for 7 classes  $\{G_i^j\}_{j=0}^6$ , where  $G_i^j$  represents the mask of the  $i$ -th image in the  $j$ -th class, and  $\{G^0\}$  denotes the annotation set for ‘others’. Using existing semantic segmentation models [25, 42], we can automatically annotate a new class in  $\{I_i\}_{i=1}^n$  to generate a set of pseudo-labels, denoted by  $\{\hat{G}_i^7\}$ . By mixing the precise labels in the MaSS13K dataset and the pseudo-labels, we obtain a new set of labels to train the model. We then design a label decoupling strategy, which employs the weighting scheme described in Sec. 4.2 to treat the labels differently. Specifically, for the precise labels annotated in MaSS13K, we emphasize the loss on edges to update the network. For pseudo-labels, we apply inverse weights to ignore potentially erroneous edge annotations, allowing the network to focus on learning the main regions of the new classes. The training loss can be expressed as follows:

$$L_{BCE}^{new} = \sum_j^{1-6} (1 + \lambda_1 W^j) L_{BCE}(P^j, G^j) + \sum_j^{0,7} (1 - \lambda_2 W^j) L_{BCE}(P^j, G^j), \quad (7)$$

where  $W^j, P^j, G^j$  represent weights map, predicted label and ground-truth label for the  $j$ -th class. In this way, we can train MaSSFormer to segment new classes one by one.

## 5. MaSS13K Benchmark

**Experiment Settings.** We present a comprehensive benchmarking on our MaSS13K dataset with existing semantic segmentation models and our MaSSFormer. We split the

13,348 images in MaSS13K into three subsets: **MaSS-train (11,348)**, **MaSS-val (500)**, and **MaSS-test (1,500)** for model training, validation, and testing, respectively. We select 14 representative and advanced semantic segmentation methods in the evaluation, which can be categorized into lightweight methods (including STDC2 [18], BeSeNetV2 [52], PIDNet [51], FeedFormer [43], SegNext [20], SeaFormer [45] and CGRSeg [38]), FCN-based methods (including DeepLabv3+ [6], UperNet [48] and OCRNet [53]), and Transformer-based methods (including MaskFormer [9], Mask2Former [7], PEM [2] and MPFormer [55]). We provide two variants of our MaSSFormer: the baseline version MaSSFormer with ResNet-50 backbone and the lightweight version MaSSFormer-Lite with ResNet-18 backbone. We implement MaSSFormer by mmsegmentation [11]. We use  $1024 \times 1024$  crops during training and use the original resolution during testing for all methods. For the competing methods, we adopt their default settings in training on our MaSS13K. More training details of our MaSSFormer can be found in **supplementary materials**.

**Evaluation Metrics.** Besides mIoU, which measures the overall segmentation accuracy, we use BIoU [8] and boundary F1-score [14] to evaluate the boundary accuracy and quality for high-resolution semantic segmentation. More details can be found in the **supplementary materials**.

### 5.1. Quantitative Evaluation

Tab. 2 shows the quantitative comparison between the proposed MaSSFormer and previous state-of-the-art semantic segmentation methods. One can see that MaSSFormer achieves the best results in terms of all the mIoU, BIoU and BF1 metrics while maintaining relatively low computational cost and parameter size, demonstrating its effectiveness and efficiency for high-resolution image segmentation. It is generally observed that correct segmentation of the main body is essential for accurate boundary segmentation, hence BIoU and BF1 tend to improve along with mIoU. However, some methods, such as FeedFormer and SegNext, show significant differences (+2.13% on MaSS13K-val) in BIoU despite having similar (-0.54%) mIoU scores. In addition, some segmentation errors in details edges and boundaries will have a small impact on the overall metrics like mIoU, but will significantly affect BIoU and BF1 scores, which can reflect a method’s capability of segmenting object details. Our MaSSFormer achieves +0.69% higher in mIoU and +1.57% higher in BIoU than the second-best method, respectively, with the same ResNet50 backbone. Meanwhile, MaSSFormer with ResNet18 backbone also demonstrates competitive performance for high-resolution image segmentation, even higher than many networks with ResNet50 backbone, but with much fewer parameters and Flops. The results of MaSSFormer on each category can be found in the **supplementary materials**.

Table 2. Quantitative evaluation on MaSS13K validation and test sets. The best and the second-best results are highlighted in **bold** and in underlined respectively. FLOPs are all calculated for an input resolution of  $4096 \times 4096$ .

Method	Ori.	Backbone	MaSS-val(500)			MaSS-test(1,500)			Model Stat.	
			mIoU $\uparrow$	BIoU $\uparrow$	BF1 $\uparrow$	mIoU $\uparrow$	BIoU $\uparrow$	BF1 $\uparrow$	Param	FLOPs
STDC2 [18]	CVPR21	-	83.08	27.99	.3334	83.76	27.72	.3332	12.30M	564G
BiSeNetv2 [52]	IJCV21	-	71.55	25.05	.3182	72.92	24.48	.3171	3.35M	591G
SegNeXt [20]	NIPS22	MSCAN-B	87.71	39.93	.4615	<u>88.11</u>	39.45	.4596	27.57M	1536G
PIDNet-L [51]	CVPR23	-	82.28	31.30	.3475	81.77	30.70	.3479	37.08M	1653G
FeedFormer [43]	AAAI23	lvt	87.17	42.06	.4838	86.56	41.07	.4789	4.65M	300G
SeaFormer-L [45]	ICLR23	-	86.78	38.61	.4498	87.36	38.28	.4489	13.95M	303G
CGRSeg-L [38]	ECCV24	EFv2-L	81.29	34.48	.4090	81.45	33.95	.4071	35.64M	1536G
DeepLabv3+ [6]	ECCV18	R50	86.66	40.08	.4718	85.14	38.65	.4678	41.22M	8008G
UperNet [48]	ECCV18	R50	82.03	35.85	.4181	81.98	35.61	.4170	64.04M	11373G
OCRNet [53]	ECCV20	R50	86.99	32.68	.3808	83.02	31.33	.3731	36.52M	7352G
MaskFormer [9]	NIPS21	R50	83.27	38.61	.4399	83.22	37.90	.4393	41.31M	2396G
Mask2Former [9]	CVPR22	R50	<u>88.28</u>	47.40	.5458	88.00	46.13	.5330	44.01M	3123G
MPFormer [55]	CVPR23	R50	87.76	<u>47.81</u>	<u>.5513</u>	87.18	<u>47.17</u>	<u>.5486</u>	43.9M	4155G
PEM [2]	CVPR24	R50	83.41	<u>40.51</u>	.4675	83.38	39.99	.4644	35.5M	1859G
MaSSFormer-Lite	-	R18	87.11	45.35	.5137	86.13	43.28	.5086	15.07M	771G
MaSSFormer	-	R50	<b>88.97</b>	<b>48.97</b>	<b>.5639</b>	<b>88.21</b>	<b>48.39</b>	<b>.5593</b>	37.42M	2036G

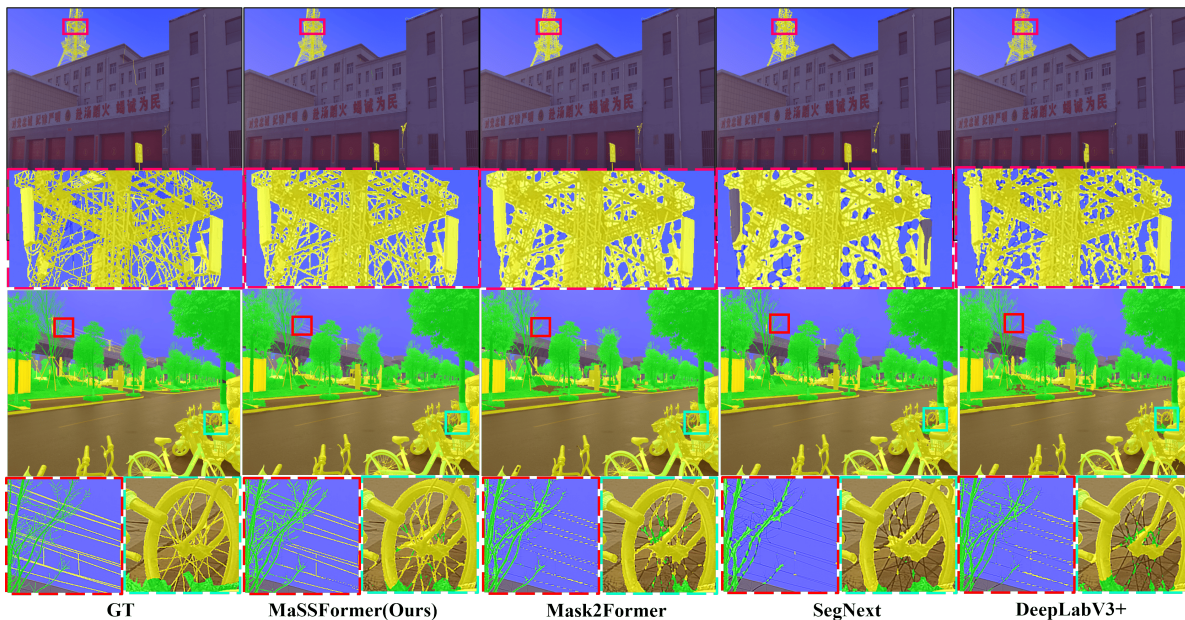


Figure 4. Qualitative comparisons of MaSSFormer with other three baseline methods. Please zoom-in for better view.

## 5.2. Qualitative Evaluation

Fig. 4 presents qualitative comparisons between our MaSSFormer and three representative methods: Mask2Former, SegNext, and DeepLabV3+, which have the best overall mIoU among the competing methods. We can see that the current methods struggle to distinguish fine details in high-resolution images, often resulting in blurry, discontinuous, or even missing segments. While this may have only a small impact on the mIoU and other metrics, it significantly degrades the visual quality and user experience of the segments. In contrast, our MaSSFormer effectively captures the details, producing higher-quality segmentation results.

Besides, MaSSFormer demonstrates high precision in various categories, including meticulous tower structures (top two rows) and thin branches and lines (bottom two rows).

**Real-world Application.** High-precision semantic image segmentation has many practical real-world applications. For example, mobile photography relies on accurate segmentation of portrait areas to achieve realistic bokeh effects. As shown in Fig. 5, the bokeh effect generated using the mask predicted by the model trained on MaSS13K is more natural and realistic than that by using the model trained on ADE20K, especially in the areas of the hands and legs. This demonstrates the importance of high-precision segmenta-



Figure 5. Comparison of bokeh effects with different masks. Please zoom-in for a better view.

Table 3. Quantitative evaluation on novel class **Car**.

Settings	Car	
	mIoU	BloU
Pseudo Label	94.18	20.44
w/o Accurate Label	92.43	22.52
w/o Label Re-weight	83.23	31.81
w Label Re-weight	95.21	35.68

tion, which depends on high-quality and high-resolution datasets such as MaSS13K.

### 5.3. Segmentation on New Class

Tab. 3 and Fig. 6 show the segmentation results of MaSSFormer on a new class, ‘Car’. The pseudo-labels generated by existing semi-automatic tools achieve high mIoU but struggle with precise edge segmentation, especially when the target and surrounding areas are visually similar. Besides, direct training with these pseudo-labels (upper-right of Fig. 6) does not improve segmentation quality. The bottom two rows of Tab. 3 show the results by mixed training with precise labels. We see that the model learns to enhance edge segmentation from precise annotations, improving the quality of car edges (see the bottom-left of Fig. 6), thus increasing BloU. However, while the car roof is accurately segmented, the surrounding regions are mistakenly classified as the ‘others’ class because the incorrect pseudo-labels in the edge region can misguide the model training, leading to a 10.95% decrease in mIoU (see the 3rd row of Tab. 3). With our re-weighting strategy, we reduce the weight of mislabeled edges, forcing the network to learn edge-aware capabilities from accurately labeled categories and new category features with higher reliability, thus achieving high-quality segmentation of new classes. More experiments can be found in the **supplementary materials**.

### 5.4. Ablation Study

We conduct a series of ablation studies to validate the effectiveness of each component of MassFormer.

**Global Semantic Aggregation.** The top 3 rows in Tab. 4 demonstrate the effectiveness of our global semantic branch. By introducing the CST module, the mIoU metric is improved by 2.57%, indicating that the acquisition of global semantics can enhance overall precision. Meanwhile, the increase in computational cost and parameters is slight. By incorporating the RFB module, the receptive field increases,

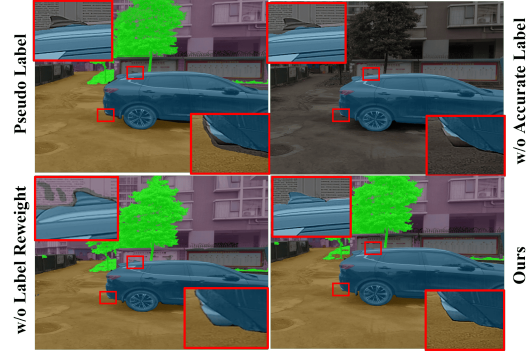


Figure 6. Visual results of MaSSFormer on novel class **Car**.

Table 4. Ablation on MaSS-val dataset.

Exp.	CST	RFB	LSE	EGF	mIoU	BloU	Para	FLOPs
#1					85.54	42.69	34.72	1298
#2	✓				88.11	44.42	35.96	1348
#3	✓	✓			88.29	45.23	37.32	1692
#4	✓	✓	✓		88.02	47.36	37.40	1928
#5	✓	✓	✓	✓	88.97	48.97	37.42	2036

leading to a further improvement in mIoU. Compared to mIoU, there is a more significant increase in BloU, indicating that our RFB module effectively fuses high-resolution features while maintaining semantic accuracy.

**Local Detail Extraction and Fusion.** Comparing Exps#3 and 4 in Tab. 4, we see that the LSE module significantly increases the BloU metric, implying that more low-level details can enhance the segmentation accuracy of edge boundaries. However, there is a slight decrease in mIoU, suggesting that direct fusion of low-level features may mislead the higher-level semantics. Exp#5 demonstrates that our designed edge-guided fusion strategy effectively improves low-level structure and high-level semantic feature fusion, resulting in an increase in both mIoU and BloU.

## 6. Conclusion

In this paper, we proposed MaSS13K and MaSSFormer for high-resolution semantic segmentation. The MaSS13K contained 13,348 real-word images at 4K resolution, with high-quality matting-level annotations in 7 categories. We then presented MaSSFormer, which efficiently aggregated global semantics and local structure details in high-resolution scenes, to address the challenges of high-resolution semantic segmentation. We compared 14 representative methods with MaSSFormer on MaSS13K, establishing a comprehensive benchmark for high-resolution semantic segmentation. Furthermore, we proposed a scheme to transfer and generalize the fine segmentation capabilities of MaSSFormer to novel classes beyond the original categories, further revealing the potential value of MaSS13K dataset. We hope that MaSS13k can advance the research on high-resolution and high-quality semantic segmentation.

# Supplementary Materials to “MaSS13K: A Matting-level Semantic Segmentation Benchmark”

In this supplementary file, we provide the following materials:

- More samples from our MaSS13K dataset (referring to Sec. 3 of the main paper).
- More details on training and evaluation metrics (referring to Sec. 5 of the main paper).
- More experimental results (referring to Sec. 5.1, 5.2, 5.3 of the main paper).
- Limitations.

## A. MaSS13K Dataset

### A.1. More Samples from MaSS13K

We provide more annotated samples from our MaSS13K in Fig. 7. MaSS13K covers a diverse range of indoor and outdoor scenes, such as urban areas, natural landscapes, street views, wilderness, parks, mall interiors, and other public spaces.

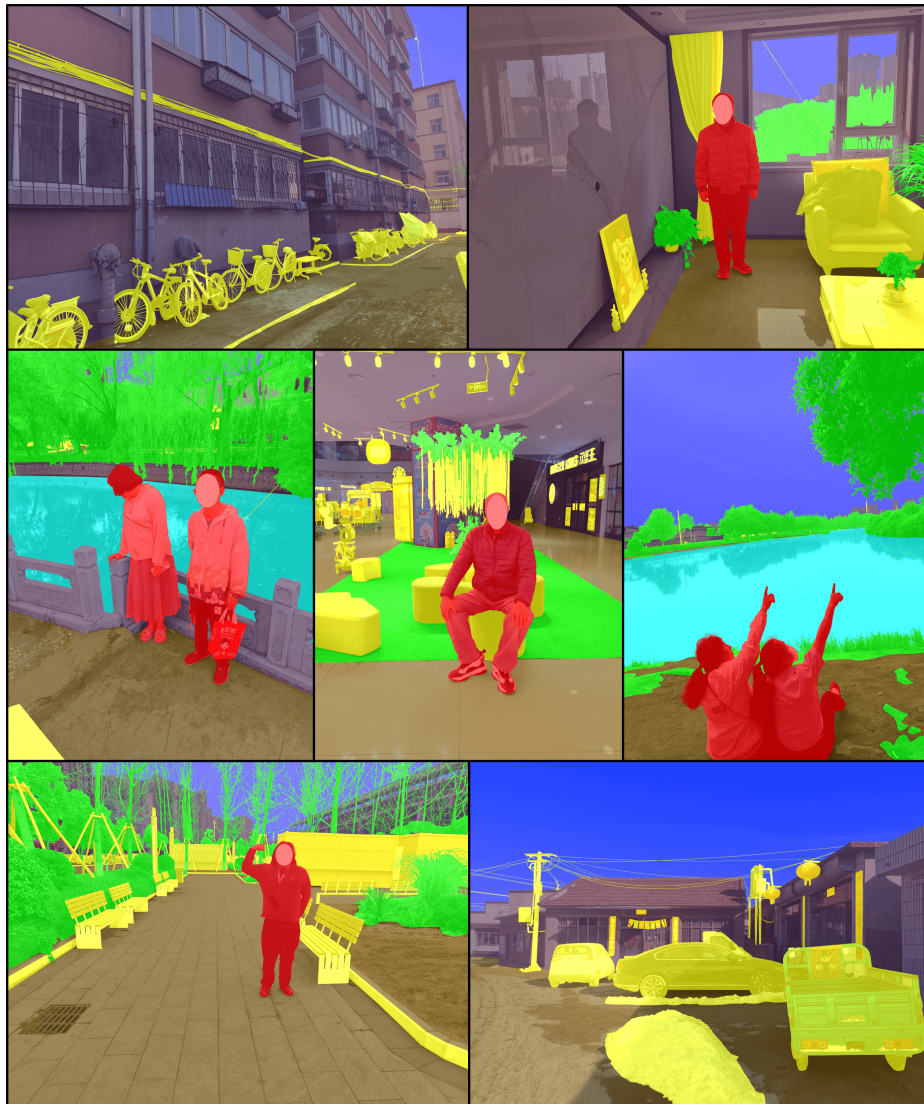


Figure 7. More samples from our MaSS13K dataset.

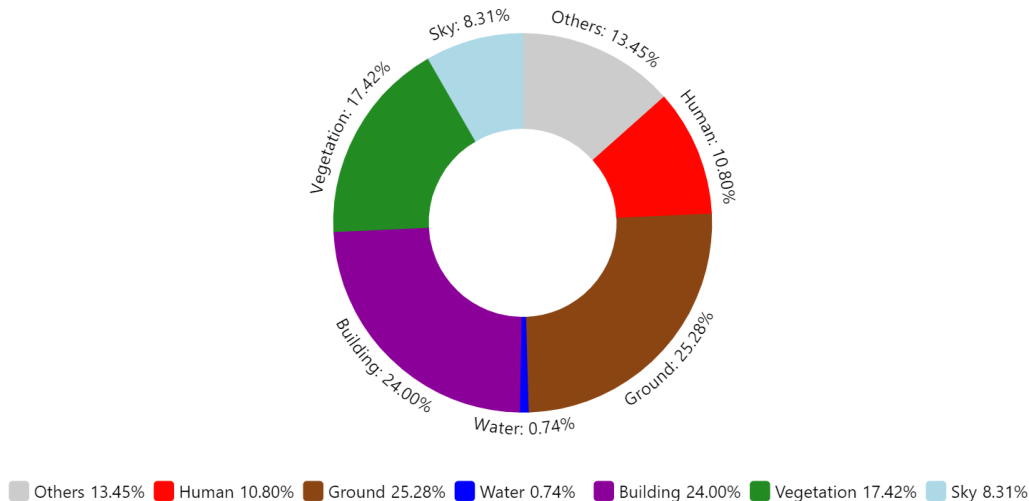


Figure 8. Pixel distribution of the seven categories in MaSS13K.

## A.2. Pixel Distribution of the Categories in MaSS13K

Fig. 8 illustrates the pixel distribution of the seven annotated categories in MaSS13K. Except for the “Water” category, the pixel distribution of the other categories is relatively balanced. The dataset primarily consists of outdoor street scenes and urban landscapes, resulting in the highest pixel proportions for “Ground” and “Building”. Additionally, 13.45% of the pixels in the dataset are classified as “Others”, which includes various objects such as traffic signs, billboards, and vehicles. Despite being grouped into the “Others” category, these objects are accurately labeled, ensuring the high quality of the dataset and its potential for further processing and development.

## B. More Details on Training and Evaluation Metrics

### B.1. Training Details

We implement MaSSFormer using mmsegmentation toolbox [11]. We use the AdamW [36] optimizer to train our model with a batch size of 16. The initial learning rate is set to 0.003 with a weight decay of 0.05, and the cosine decay schedule is applied during training. For data augmentation, we mainly follow the setup of Mask2Former [7], including random resizing, random cropping, and random flipping. The models are trained for 80k iterations on the MaSS13K dataset.

For the other evaluated methods on the MaSS13K dataset, we use their default settings on learning rate and data augmentation. The resolution during training and testing for all methods is kept consistent to ensure a fair comparison. The number of parameters and FLOPs for all methods are calculated using the mmsegmentation tools, except for PEM and MPFormer, which are calculated using Detectron2 tools.

### B.2. Details of Evaluation Metrics

In high-resolution semantic segmentation, there are numerous fine-grained regions of object details that are critical for the quality of the segmentation masks. However, the standard mask IoU metric is too coarse to differentiate these fine-grained regions, making it less effective in evaluating high-resolution semantic segmentation performance. To better evaluate and compare the methods of high-resolution semantic segmentation, we also use boundary-focused metrics, including Boundary IoU (BIOU) [8] and Boundary F-1 Score (BF1) [14], in the main paper.

**BIOU.** For the mask of the  $i$ -th category, the  $\text{BIOU}^i$  is defined as follows:

$$\text{BIOU}^i = \frac{(G_d^i \cap G^i) \cap (P_d^i \cap P^i)}{(G_d^i \cap G^i) \cup (P_d^i \cap P^i)}, \quad (8)$$

where  $P$  and  $G$  denote the predicted and ground-truth maps, respectively, and the subscript  $d$  denotes the mask obtained by dilating the boundary by  $d$  pixels. In our benchmark, we set  $d$  to 0.1% of the diagonal length, which is 5 pixels, to better measure the accuracy of details.

**BF1.** BF1 Score is a commonly used evaluation metric for edge detection and segmentation that combines precision and recall to assess the edge quality of a segmentation map. The BF1 score is calculated as follows:

$$BF1 = 2 \times \frac{\text{Precision} \times \text{Recall}}{\text{Precision} + \text{Recall}}, \tag{9}$$

where Precision =  $\frac{TP}{TP+FP}$  and Recall =  $\frac{TP}{TP+FN}$ . In this case, if a point of predicted boundary matches a ground truth boundary point within a distance error tolerance, it is considered a true positive. In our evaluation, we set the distance error tolerance to 2. “TP + FP” can be represented by the total number of edge points in the ground truth map, and “TP + FN” can be represented by the total number of edge points in prediction map.

## C. More Experimental Results

### C.1. Ablation on Different Backbones

In Tab. 5, we compare the performance of Mask2Former and MaSSFormer using stronger backbones. We can observe that with stronger backbones, the IoU scores become higher due to the improved global semantic extraction capabilities. However, the BIoU and BF1 gaps between Mask2Former and our proposed MaSSFormer are enlarged, further validating that MaSSFormer can better process detail regions and produce higher-quality segmentation edges.

Methods	Backbone	MaSS-val			MaSS-test			Stat.	
		mIoU	BIoU	BF1	mIoU	BIoU	BF1	Para.	FLOPS
Mask2Former	Swin-T	89.17	48.27	0.5529	89.47	47.97	0.5509	47.40M	3148G
MaSSFormer	Swin-T	89.49 (+0.32)	49.68 (+1.41)	0.5719 (+0.0190)	89.40 (-0.07)	49.50 (+1.53)	0.5685 (+0.0176)	40.92M	1956G
Mask2Former	Swin-B	91.30	51.20	0.5912	91.10	50.83	0.5893	107M	6126G
MaSSFormer	Swin-B	91.35 (+0.05)	53.00 (+1.80)	0.6102 (+0.0190)	91.31 (+0.21)	52.74 (+1.91)	0.6076 (+0.0183)	100M	4890G

Table 5. Quantitative comparison with different backbones.

### C.2. Results of Each Category

In Tab. 6 and Tab. 7, we present detailed quantitative results for each category in **MaSS-val** and **MaSS-test**, respectively. From the two tables, it is evident that the ‘Others’ class has the lowest IoU scores. This is because the ‘Others’ class aggregates a variety of objects beyond the six categories, making it more challenging to identify and leading to lower overall IoU. In contrast, the ‘Human’ and ‘Sky’ categories are relatively distinct and well-defined, resulting in higher IoU scores. Additionally, we observe that MaSSFormer achieves the most significant improvement in BIoU for the ‘Vegetation’ category compared to other methods. This aligns with our visual observations, as trees in the dataset contain a large amount of boundaries and details.

### C.3. More Details and Results on Segmenting New Classes

**Details of the Pipeline.** We utilize the Grounded-SAM [42] as a semi-automatic labeling tool to obtain pseudo labels without human effort. Grounded-SAM employs the bounding boxes from Grounding-DINO [32] as the input to SAM [25] to generate masks for the corresponding objects. Grounding-DINO, as an open-vocabulary detection model, can take any text prompt and produce bounding boxes for objects of that category in the image. Therefore, for a new category ‘X’, we input ‘X’ as a text-prompt into Grounded-SAM, process all images in the dataset to obtain instance segmentation masks for that category, and then merge and convert these masks into semantic segmentation labels for the new category ‘X’. We combine the semantic labels of the new category with the existing seven categories’ labels for joint model training. To provide a quantitative evaluation of the mask quality for the new category, we manually annotate a set of images of that category from the test set to calculate the mIoU, BIoU, and BF1 scores. What’s more, in the training on new categories, we uniformly use a crop size of 2048x2048.

**More Results.** In the main paper, we have validated the effectiveness of our method in segmenting a new class ‘Car’ on MaSS13K. In this supplementary file, we conduct experiments on another new class ‘Bicycle’. The results are shown in Tab. 8. For the convenience of readers, we also put the results of class ‘Car’ in the table. We can see that for both of the

Table 6. Quantitative evaluation on MaSS-val for each category.

Methods	Others			Human			Building			Vegetation			Ground			Sky			Water		
	mIoU	BloU	BF1	mIoU	BloU	BF1	mIoU	BloU	BF1	mIoU	BloU	BF1	mIoU	BloU	BF1	mIoU	BloU	BF1	mIoU	BloU	BF1
STDC2	66.52	18.39	.2041	95.77	45.06	.5366	77.96	19.78	.2467	87.88	22.84	.2701	90.62	32.54	.4311	89.96	34.21	.3647	73.51	23.66	.2582
BiSeNetV2	53.26	13.31	.1589	92.38	38.90	.5087	69.93	15.27	.2013	83.62	27.45	.3013	85.16	26.84	.3940	82.90	41.45	.4637	35.83	11.40	.1417
SegNext	70.17	25.37	.3050	97.58	59.61	.7061	82.22	27.68	.3440	89.30	36.58	.4132	93.74	40.94	.5392	92.40	48.89	.5783	88.60	40.50	.4462
PIDNet-L	64.71	19.83	.2258	96.16	44.74	.4597	77.74	21.82	.2620	86.64	29.74	.3278	89.84	32.24	.4324	89.64	41.85	.4515	71.15	28.90	.3144
FeedFormer	65.90	23.34	.2870	97.02	57.68	.6986	79.46	26.97	.3465	89.67	44.59	.5006	92.66	38.93	.5187	94.10	62.19	.7321	91.42	40.73	.4464
SeaFormer	69.75	24.53	.2918	97.10	57.88	.7029	82.63	26.93	.3349	88.41	34.61	.3955	92.16	39.69	.5211	93.59	48.56	.5565	83.83	38.13	.4279
CGRSeg	59.32	21.83	.2618	90.42	47.90	.6129	74.05	23.42	.2917	88.15	34.30	.3843	87.47	34.53	.4699	88.88	46.60	.5486	80.80	32.78	.4031
DeepLabV3+	67.61	22.76	.2947	96.30	56.36	.7074	78.83	25.30	.3359	89.35	41.46	.4831	90.25	34.66	.4935	94.09	60.35	.6822	90.28	40.38	.4518
UperNet	62.60	20.15	.2554	92.60	45.40	.5772	77.32	23.63	.2941	88.20	39.85	.4479	88.79	33.03	.4553	91.44	58.36	.6253	73.46	31.39	.3456
OCRNet	61.11	18.34	.2304	93.91	46.63	.6051	75.17	20.19	.2617	88.22	31.15	.3577	89.35	31.17	.4398	92.45	47.05	.5077	87.78	34.61	.3548
MaskFormer	60.16	19.82	.2680	94.55	51.09	.6463	72.94	22.80	.3043	87.83	43.98	.4844	85.69	29.78	.4303	93.96	62.15	.7159	87.72	40.65	.4194
Mask2Former	72.45	31.23	.3907	98.13	66.08	.7755	82.95	32.86	.4165	90.25	45.99	.5170	93.23	44.72	.5824	94.52	63.59	.7417	86.42	47.35	.5241
MPPFormer	73.34	31.84	.3913	98.49	67.49	.7885	84.29	33.93	.4258	89.93	46.90	.5305	93.04	44.68	.5772	93.59	64.29	.7475	81.68	45.54	.5139
PEM	68.10	25.46	.3198	97.50	60.32	.7288	70.49	23.61	.3232	89.75	44.25	.4929	77.71	26.98	.4225	93.31	61.66	.7171	87.02	41.30	.4480
MaSSFormer-Lite	67.62	26.02	.3288	96.98	61.01	.7352	79.65	30.01	.3854	88.90	49.31	.5374	90.59	38.90	.5327	95.35	68.26	.7587	90.65	43.97	.4784
MaSSFormer	71.27	30.84	.3931	97.44	64.62	.7783	82.74	33.74	.4385	89.76	50.36	.5799	93.40	44.13	.5605	95.90	69.91	.8108	92.32	49.18	.5594

Table 7. Quantitative evaluation on MaSS-test for each category.

Methods	Others			Human			Building			Vegetation			Ground			Sky			Water		
	mIoU	BloU	mIoU	BF1	BloU	mIoU	BF1	BloU	mIoU	BF1	BloU	mIoU	BF1	BloU	mIoU	BF1	BloU	mIoU	BF1	BloU	BF1
STDC2	66.75	17.88	.2008	94.98	43.71	.5246	78.97	19.69	.2492	87.72	22.36	.2680	90.35	31.82	.4302	91.20	34.27	.3712	76.37	24.29	.2622
BiSeNetV2	52.63	12.84	.1600	90.53	37.35	.4967	70.37	15.24	.2010	83.31	26.91	.2979	84.90	26.45	.3934	86.50	41.27	.4625	42.23	11.27	.1500
SegNext	69.80	24.63	.3031	97.41	58.45	.6935	82.40	27.45	.3472	89.41	36.24	.4076	93.49	39.78	.5316	93.50	49.49	.5775	90.76	40.12	.4490
PIDNet-L	64.63	19.65	.2269	95.47	43.50	.4505	78.24	22.13	.2668	87.07	29.38	.3210	89.69	31.77	.4304	89.95	42.08	.4586	67.31	26.38	.3191
FeedFormer	65.67	22.47	.2823	96.29	55.91	.6824	79.82	26.70	.3464	89.55	44.06	.4898	92.34	37.80	.5138	94.29	62.28	.7281	88.02	38.31	.4457
SeaFormer	69.30	24.23	.2927	96.23	56.49	.6923	82.68	27.04	.3373	88.66	34.30	.3883	92.13	38.77	.5172	93.61	48.96	.5556	88.96	38.23	.4354
CGRSeg	59.17	21.09	.2596	90.65	46.80	.6038	73.96	23.37	.2952	87.97	33.82	.3778	87.68	33.78	.4686	90.64	46.92	.5426	80.09	31.92	.3942
DeepLabV3+	67.32	22.46	.2930	95.65	54.11	.6906	79.25	25.66	.3363	89.35	41.53	.4763	89.76	33.95	.4859	93.37	60.16	.6816	81.25	32.65	.4224
UperNet	61.97	19.78	.2515	90.70	43.30	.5601	77.74	24.19	.3000	88.20	40.29	.4429	88.20	32.56	.4500	92.19	59.08	.6318	74.87	30.06	.3617
OCRNet	60.60	17.57	.2222	92.41	43.44	.5875	75.76	20.08	.2580	87.74	30.36	.3437	88.48	29.83	.4306	92.65	46.95	.5070	83.56	31.10	.3501
MaskFormer	61.28	19.65	.2679	94.48	50.26	.6430	74.64	22.99	.3059	88.24	44.14	.4818	85.61	29.04	.4241	94.25	62.80	.7160	84.06	36.45	.4182
Mask2Former	70.67	29.60	.3708	97.69	65.02	.7656	80.83	31.94	.4033	90.25	44.37	.4985	91.66	42.60	.5608	94.88	64.13	.7241	90.00	45.27	.5233
MPPFormer	72.38	31.23	.3896	98.06	66.13	.7784	83.91	33.67	.4271	90.17	46.70	.5228	92.58	43.68	.5718	93.57	64.81	.7451	79.63	44.02	.5124
PEM	67.70	25.04	.3210	97.46	59.97	.7205	72.14	24.02	.3287	89.12	44.01	.4854	78.75	26.12	.4146	91.86	61.25	.7094	86.69	39.51	.4593
MaSSFormer-Lite	66.80	25.11	.3260	96.39	59.19	.7216	79.60	29.55	.3844	88.77	46.75	.5280	90.87	37.69	.5170	94.77	64.54	.7548	85.71	40.08	.4707
MaSSFormer	70.07	29.70	.3860	97.23	64.02	.7665	81.65	33.40	.4387	90.03	51.91	.5772	91.51	41.56	.5557	95.60	70.30	.8043	90.18	47.82	.5611

two new classes, the IoU, BloU, and BF1 metrics show significant improvements over the baseline. Some visual examples of the segmentation results of ‘Bicycle’ are presented in Fig. 9. We can see that due to the relatively small size of bicycle targets, the incorrect segmentation of the wheels can severely impact the IoU scores, as shown in the 2nd row of Fig. 9. In addition, the failure of Grounded-SAM to detect small targets can further reduce the IoU, as illustrated in the 1st row of Fig. 9. Our method, designed for high-resolution images, can effectively capture fine structural details and boundaries, resulting in higher IoU and BF1 scores. Furthermore, under the joint supervision of other precise categories, our method can accurately distinguish foreground from background at the wheel areas, resulting in precise segmentation of the target objects.

#### C.4. More Qualitative Comparisons

We present more qualitative comparisons between our MaSSFormer and other representative methods in Fig. 10. It can be seen that MaSSFormer demonstrates superior performance in segmenting fine-grained regions, such as the thin lines in the 1st image. It maintains accurate segmentation even for small objects in the distance (the 3rd image). For fine structures such as hair, the competing methods often fail to achieve fine-level segmentation and tend to predict the surrounding areas

Table 8. Quantitative evaluation on novel classes **Bicycle** and **Car**.

Settings	<b>Bicycle</b>			<b>Car</b>		
	mIoU	BIoU	BF1	mIoU	BIoU	BF1
Pseudo label generated by Grounded-SAM	49.40	23.82	0.2800	94.18	20.44	0.2522
Prediction generated by our joint-trained model	74.57	40.17	0.4609	95.21	35.68	0.3643

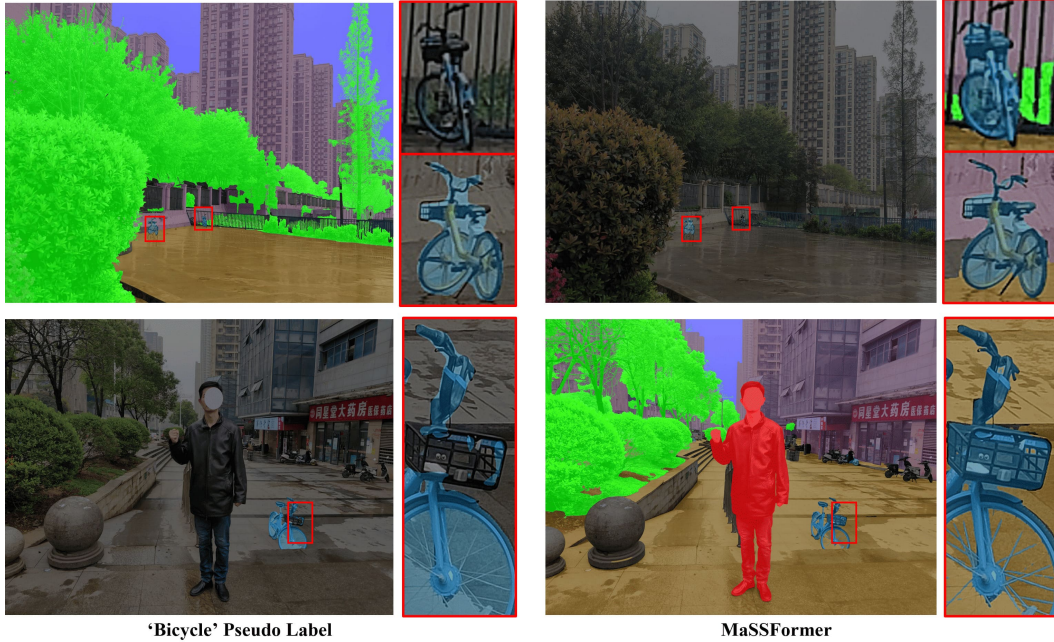


Figure 9. Visual results on the segmentation of ‘Bicycle’ class. Left: Pseudo-labels generated by Grounded-SAM. Right: Predictions by MaSSFormer.

as hair (the 2nd and 4th images). In contrast, MaSSFormer effectively distinguishes hair and other detailed elements from the background, ensuring high-quality segmentation.

### D. Limitations

First, while MaSS13K provides 13K finely annotated images, it can be further expanded in the number of samples, scenes, and categories. Second, although MaSSFormer has achieved a relatively good balance between accuracy and efficiency, its computational cost and memory usage are still high, especially for mobile devices. New lightweight networks are expected for efficient yet accurate high-resolution semantic segmentation.

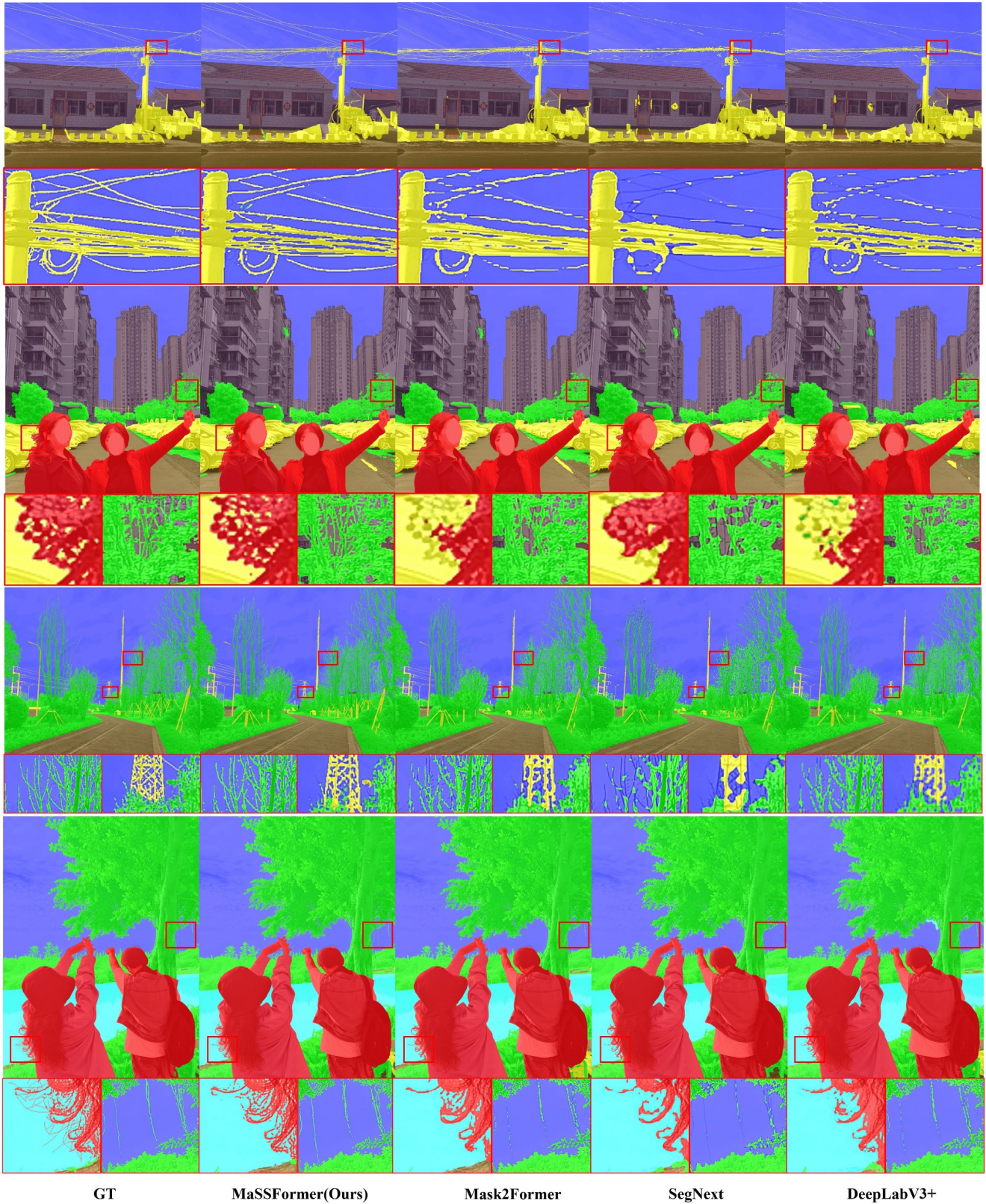


Figure 10. More qualitative comparisons between MaSSFormer and other methods. Please zoom-in for a better view.

## References

- [1] Nicolas Carion, Francisco Massa, Gabriel Synnaeve, Nicolas Usunier, Alexander Kirillov, and Sergey Zagoruyko. End-to-end object detection with transformers. In *ECCV*, 2020. [3](#)
- [2] Niccolò Cavagnero, Gabriele Rosi, Claudia Cuttano, Francesca Pistilli, Marco Ciccone, Giuseppe Averta, and Fabio Cermelli. Pem: Prototype-based efficient maskformer for image segmentation. In *Proceedings of the IEEE/CVF Conference on Computer Vision and Pattern Recognition*, pages 15804–15813, 2024. [2](#), [3](#), [4](#), [6](#), [7](#)
- [3] Liang-Chieh Chen. Semantic image segmentation with deep convolutional nets and fully connected crfs. *arXiv preprint arXiv:1412.7062*, 2014. [3](#)
- [4] Liang-Chieh Chen, George Papandreou, Iasonas Kokkinos, Kevin Murphy, and Alan L Yuille. Deeplab: Semantic image segmentation with deep convolutional nets, atrous convolution, and fully connected crfs. *IEEE transactions on pattern analysis and machine intelligence*, 40(4):834–848, 2017.
- [5] Liang-Chieh Chen, George Papandreou, Florian Schroff, and Hartwig Adam. Rethinking atrous convolution for semantic image segmentation. *arXiv:1706.05587*, 2017. [2](#), [3](#)
- [6] Liang-Chieh Chen, Yukun Zhu, George Papandreou, Florian Schroff, and Hartwig Adam. Encoder-decoder with atrous separable convolution for semantic image segmentation. In *ECCV*, 2018. [2](#), [5](#), [6](#), [7](#)
- [7] Bowen Cheng, Anwesa Choudhuri, Ishan Misra, Alexander Kirillov, Rohit Girdhar, and Alexander G Schwing. Mask2former for video instance segmentation. *arXiv preprint arXiv:2112.10764*, 2021. [2](#), [3](#), [4](#), [5](#), [6](#), [10](#)
- [8] Bowen Cheng, Ross Girshick, Piotr Dollár, Alexander C Berg, and Alexander Kirillov. Boundary iou: Improving object-centric image segmentation evaluation. In *Proceedings of the IEEE/CVF Conference on Computer Vision and Pattern Recognition*, 2021. [6](#), [10](#)
- [9] Bowen Cheng, Alex Schwing, and Alexander Kirillov. Pixel classification is not all you need for semantic segmentation. *NeurIPS*, 2021. [2](#), [3](#), [5](#), [6](#), [7](#)
- [10] Ho Kei Cheng, Jihoon Chung, Yu-Wing Tai, and Chi-Keung Tang. Cascadepsp: Toward class-agnostic and very high-resolution segmentation via global and local refinement. In *Proceedings of the IEEE/CVF conference on computer vision and pattern recognition*, pages 8890–8899, 2020. [3](#), [4](#)
- [11] MMSegmentation Contributors. MMSegmentation: Openmmlab semantic segmentation toolbox and benchmark. <https://github.com/open-mmlab/mms Segmentation>, 2020. [6](#), [10](#)
- [12] Marius Cordts, Mohamed Omran, Sebastian Ramos, Timo Rehfeld, Markus Enzweiler, Rodrigo Benenson, Uwe Franke, Stefan Roth, and Bernt Schiele. The cityscapes dataset for semantic urban scene understanding. In *Proceedings of the IEEE conference on computer vision and pattern recognition*, pages 3213–3223, 2016. [3](#), [4](#)
- [13] Guillaume Couairon, Jakob Verbeek, Holger Schwenk, and Matthieu Cord. Diffedit: Diffusion-based semantic image editing with mask guidance. *arXiv preprint arXiv:2210.11427*, 2022. [2](#)
- [14] Gabriela Csurka, Diane Larlus, Florent Perronnin, and France Meylan. What is a good evaluation measure for semantic segmentation?. In *Bmvc*, pages 10–5244. Bristol, 2013. [6](#), [10](#)
- [15] Omar Elharrouss, Somaya Al-Maadeed, Nandhini Subramanian, Najmath Ottakath, Noor Almaadeed, and Yassine Himeur. Panoptic segmentation: A review. *arXiv preprint arXiv:2111.10250*, 2021. [3](#)
- [16] Mark Everingham, Luc Van Gool, Christopher KI Williams, John Winn, and Andrew Zisserman. The pascal visual object classes (voc) challenge. *IJCV*, 2010. [3](#), [4](#)
- [17] Deng-Ping Fan, Ge-Peng Ji, Guolei Sun, Ming-Ming Cheng, Jianbing Shen, and Ling Shao. Camouflaged object detection. In *Proceedings of the IEEE/CVF conference on computer vision and pattern recognition*, pages 2777–2787, 2020. [3](#)
- [18] Mingyuan Fan, Shenqi Lai, Junshi Huang, Xiaoming Wei, Zhenhua Chai, Junfeng Luo, and Xiaolin Wei. Rethinking bisenet for real-time semantic segmentation. In *Proceedings of the IEEE/CVF conference on computer vision and pattern recognition*, pages 9716–9725, 2021. [2](#), [6](#), [7](#)
- [19] Alberto Garcia-Garcia, Sergio Orts-Escolano, Sergiu Oprea, Victor Villena-Martinez, and Jose Garcia-Rodriguez. A review on deep learning techniques applied to semantic segmentation. *arXiv preprint arXiv:1704.06857*, 2017. [3](#)
- [20] Meng-Hao Guo, Cheng-Ze Lu, Qibin Hou, Zhengning Liu, Ming-Ming Cheng, and Shi-Min Hu. Segnext: Rethinking convolutional attention design for semantic segmentation. *Advances in Neural Information Processing Systems*, 35:1140–1156, 2022. [2](#), [6](#), [7](#)
- [21] Abdul Mueed Hafiz and Ghulam Mohiuddin Bhat. A survey on instance segmentation: state of the art. *International journal of multimedia information retrieval*, 9(3):171–189, 2020. [3](#)
- [22] Jie Hu, Li Shen, and Gang Sun. Squeeze-and-excitation networks. In *Proceedings of the IEEE conference on computer vision and pattern recognition*, pages 7132–7141, 2018. [4](#)
- [23] Andrey Ignatov, Jagruti Patel, and Radu Timofte. Rendering natural camera bokeh effect with deep learning. In *Proceedings of the IEEE/CVF Conference on Computer Vision and Pattern Recognition Workshops*, pages 418–419, 2020. [2](#)
- [24] Zhanghan Ke, Jiayu Sun, Kaican Li, Qiong Yan, and Rynson W.H. Lau. Modnet: Real-time trimap-free portrait matting via objective decomposition. In *AAAI*, 2022. [2](#)
- [25] Alexander Kirillov, Eric Mintun, Nikhila Ravi, Hanzi Mao, Chloe Rolland, Laura Gustafson, Tete Xiao, Spencer Whitehead, Alexander C Berg, Wan-Yen Lo, et al. Segment anything. In *Proceedings of the IEEE/CVF International Conference on Computer Vision*, pages 4015–4026, 2023. [6](#), [11](#)
- [26] Tae-young Ko and Seung-ho Lee. Novel method of semantic segmentation applicable to augmented reality. *Sensors*, 20(6):1737, 2020. [2](#)
- [27] Anat Levin, Dani Lischinski, and Yair Weiss. A closed-form solution to natural image matting. *IEEE transactions on pattern analysis and machine intelligence*, 30(2):228–242, 2007. [2](#)

- [28] Jizhizi Li, Jing Zhang, and Dacheng Tao. Deep automatic natural image matting. *arXiv preprint arXiv:2107.07235*, 2021. [2](#), [3](#)
- [29] Xiangtai Li, Xia Li, Li Zhang, Guangliang Cheng, Jianping Shi, Zhouchen Lin, Shaohua Tan, and Yunhai Tong. Improving semantic segmentation via decoupled body and edge supervision. In *Computer Vision—ECCV 2020: 16th European Conference, Glasgow, UK, August 23–28, 2020, Proceedings, Part XVII 16*, pages 435–452. Springer, 2020. [3](#)
- [30] Tsung-Yi Lin, Michael Maire, Serge Belongie, James Hays, Pietro Perona, Deva Ramanan, Piotr Dollár, and C Lawrence Zitnick. Microsoft coco: Common objects in context. In *Computer Vision—ECCV 2014: 13th European Conference, Zurich, Switzerland, September 6–12, 2014, Proceedings, Part V 13*, pages 740–755. Springer, 2014. [1](#), [3](#), [4](#)
- [31] Tsung-Yi Lin, Piotr Dollár, Ross Girshick, Kaiming He, Bharath Hariharan, and Serge Belongie. Feature pyramid networks for object detection. In *CVPR*, 2017. [2](#)
- [32] Shilong Liu, Zhaoyang Zeng, Tianhe Ren, Feng Li, Hao Zhang, Jie Yang, Chunyuan Li, Jianwei Yang, Hang Su, Jun Zhu, et al. Grounding dino: Marrying dino with grounded pre-training for open-set object detection. *arXiv preprint arXiv:2303.05499*, 2023. [11](#)
- [33] Ze Liu, Yutong Lin, Yue Cao, Han Hu, Yixuan Wei, Zheng Zhang, Stephen Lin, and Baining Guo. Swin transformer: Hierarchical vision transformer using shifted windows. In *Proceedings of the IEEE/CVF International Conference on Computer Vision*, 2021. [2](#)
- [34] Zerun Liu, Fan Zhang, Jingxuan He, Jin Wang, Zhangye Wang, and Lechao Cheng. Text-guided mask-free local image retouching. In *2023 IEEE International Conference on Multimedia and Expo (ICME)*, pages 2783–2788. IEEE, 2023. [2](#)
- [35] Jonathan Long, Evan Shelhamer, and Trevor Darrell. Fully convolutional networks for semantic segmentation. In *CVPR*, 2015. [2](#), [3](#)
- [36] I Loshchilov. Decoupled weight decay regularization. *arXiv preprint arXiv:1711.05101*, 2017. [10](#)
- [37] Gerhard Neuhold, Tobias Ollmann, Samuel Rota Buló, and Peter Kotschieder. The mapillary vistas dataset for semantic understanding of street scenes. In *ICCV*, 2017. [2](#), [3](#)
- [38] Zhenliang Ni, Xinghao Chen, Yingjie Zhai, Yehui Tang, and Yunhe Wang. Context-guided spatial feature reconstruction for efficient semantic segmentation. *arXiv preprint arXiv:2405.06228*, 2024. [2](#), [6](#), [7](#)
- [39] Robert Osserman. The isoperimetric inequality. *Bulletin of the American Mathematical Society*, 84(6):1182–1238, 1978. [2](#), [4](#)
- [40] Lu Qi, Jason Kuen, Weidong Guo, Tiancheng Shen, Jiuxiang Gu, Jiaya Jia, Zhe Lin, and Ming-Hsuan Yang. High-quality entity segmentation. *arXiv preprint arXiv:2211.05776*, 2022. [2](#), [3](#), [4](#)
- [41] Xuebin Qin, Hang Dai, Xiaobin Hu, Deng-Ping Fan, Ling Shao, and Luc Van Gool. Highly accurate dichotomous image segmentation. In *European Conference on Computer Vision*, pages 38–56. Springer, 2022. [2](#), [3](#), [4](#)
- [42] Tianhe Ren, Shilong Liu, Ailing Zeng, Jing Lin, Kunchang Li, He Cao, Jiayu Chen, Xinyu Huang, Yukang Chen, Feng Yan, Zhaoyang Zeng, Hao Zhang, Feng Li, Jie Yang, Hongyang Li, Qing Jiang, and Lei Zhang. Grounded sam: Assembling open-world models for diverse visual tasks, 2024. [6](#), [11](#)
- [43] Jae-hun Shim, Hyunwoo Yu, Kyeongbo Kong, and Suk-Ju Kang. Feedformer: Revisiting transformer decoder for efficient semantic segmentation. In *Proceedings of the AAAI Conference on Artificial Intelligence*, pages 2263–2271, 2023. [2](#), [6](#), [7](#)
- [44] Ashish Vaswani, Noam Shazeer, Niki Parmar, Jakob Uszkoreit, Llion Jones, Aidan N Gomez, Łukasz Kaiser, and Illia Polosukhin. Attention is all you need. In *NeurIPS*, 2017. [2](#)
- [45] Qiang Wan, Zilong Huang, Jiachen Lu, YU Gang, and Li Zhang. Seaformer: Squeeze-enhanced axial transformer for mobile semantic segmentation. In *The eleventh international conference on learning representations*, 2023. [2](#), [6](#), [7](#)
- [46] Chi Wang, Yunke Zhang, Miaomiao Cui, Peiran Ren, Yin Yang, Xuansong Xie, Xian-Sheng Hua, Hujun Bao, and Weiwei Xu. Active boundary loss for semantic segmentation. In *Proceedings of the AAAI Conference on Artificial Intelligence*, pages 2397–2405, 2022. [3](#)
- [47] Sanghyun Woo, Jongchan Park, Joon-Young Lee, and In So Kweon. Cbam: Convolutional block attention module. In *Proceedings of the European conference on computer vision (ECCV)*, pages 3–19, 2018. [5](#)
- [48] Tete Xiao, Yingcheng Liu, Bolei Zhou, Yuning Jiang, and Jian Sun. Unified perceptual parsing for scene understanding. In *Proceedings of the European conference on computer vision (ECCV)*, pages 418–434, 2018. [2](#), [6](#), [7](#)
- [49] Chenxi Xie, Changqun Xia, Mingcan Ma, Zhirui Zhao, Xiaowu Chen, and Jia Li. Pyramid grafting network for one-stage high resolution saliency detection. In *Proceedings of the IEEE/CVF conference on computer vision and pattern recognition*, pages 11717–11726, 2022. [3](#), [4](#)
- [50] Chenxi Xie, Changqun Xia, Tianshu Yu, and Jia Li. Frequency representation integration for camouflaged object detection. In *Proceedings of the 31st ACM International Conference on Multimedia*, page 1789–1797, New York, NY, USA, 2023. Association for Computing Machinery. [3](#)
- [51] Jiacong Xu, Zixiang Xiong, and Shankar P Bhattacharyya. Pidnet: A real-time semantic segmentation network inspired by pid controllers. In *Proceedings of the IEEE/CVF conference on computer vision and pattern recognition*, pages 19529–19539, 2023. [2](#), [3](#), [6](#), [7](#)
- [52] Changqian Yu, Changxin Gao, Jingbo Wang, Gang Yu, Chunhua Shen, and Nong Sang. Bisenet v2: Bilateral network with guided aggregation for real-time semantic segmentation. *International journal of computer vision*, 129: 3051–3068, 2021. [3](#), [6](#), [7](#)
- [53] Yuhui Yuan, Xilin Chen, and Jingdong Wang. Object-contextual representations for semantic segmentation. In *Computer Vision—ECCV 2020: 16th European Conference, Glasgow, UK, August 23–28, 2020, Proceedings, Part VI 16*, pages 173–190. Springer, 2020. [2](#), [3](#), [6](#), [7](#)
- [54] Yi Zeng, Pingping Zhang, Jianming Zhang, Zhe Lin, and Huchuan Lu. Towards high-resolution salient object detection. In *Proceedings of the IEEE/CVF international conference on computer vision*, pages 7234–7243, 2019. [3](#), [4](#)

- [55] Hao Zhang, Feng Li, Huaizhe Xu, Shijia Huang, Shilong Liu, Lionel M Ni, and Lei Zhang. Mp-former: Mask-piloted transformer for image segmentation. In *Proceedings of the IEEE/CVF Conference on Computer Vision and Pattern Recognition*, pages 18074–18083, 2023. [2](#), [6](#), [7](#)
- [56] Hengshuang Zhao, Jianping Shi, Xiaojuan Qi, Xiaogang Wang, and Jiaya Jia. Pyramid scene parsing network. In *CVPR*, 2017. [3](#), [4](#)
- [57] Bolei Zhou, Hang Zhao, Xavier Puig, Sanja Fidler, Adela Barriuso, and Antonio Torralba. Scene parsing through ade20k dataset. In *Proceedings of the IEEE conference on computer vision and pattern recognition*, pages 633–641, 2017. [1](#), [3](#), [4](#)